


Pore-scale study of convective mixing process in brine sequestration of impure CO₂

Long Ju ^{1,2}, Baochao Shan,³ and Zhaoli Guo^{4,*}

¹*Yantai Research Institute of Harbin Engineering University, Yantai 264000, China*

²*State Key Laboratory of Coal Combustion, School of Energy and Power Engineering, Huazhong University of Science and Technology, Wuhan 430074, China*

³*School of Engineering, The University of Edinburgh, Edinburgh EH9 3FB, United Kingdom*

⁴*Institute of Interdisciplinary Research for Mathematics and Applied Science, Huazhong University of Science and Technology, Wuhan 430074, China*



(Received 21 May 2022; accepted 4 November 2022; published 21 November 2022)

Impurities such as H₂S and SO₂ play important roles in dissolution trapping mechanisms in geological sequestration of CO₂. In this study, a pore-scale numerical investigation of the convective mixing process in geological storage is conducted using the lattice Boltzmann method. Tests with a different value of diffusivity ratio R_D and buoyancy ratio of the impurities $R_\beta R_C$ are considered. Theoretical analysis demonstrates four distinct scenarios of initial diffusive density distribution, including the monotonic and nonmonotonic density distributions along the gravity direction. Numerical results show that the general phenomena of the mixing processes are quite different in different scenarios. In particular, when the density distribution is nonmonotonic, the intensity of the system's convective mixing will be weakened by the density stratification structure. At the same time, the time evolution of the dissolution flux is also affected by impurities correspondingly, leading to some differences from the pure-CO₂ system. In addition, the onset times of convection for different impure systems are also investigated. For a given Rayleigh number, the system is less prone to gravitational instability compared to that with only CO₂, when $R_\beta R_C < 0$ and the onset time will be prolonged correspondingly. In order to assess the strength of convection in an impure system, an effective Rayleigh number Ra_e is defined in this paper, where the influences of impurities are taken into account. According to the simulation results, the onset time t_{on} can be well fitted as $t_{on} \sim Ra_e^{-2}$, which is consistent with the role of the Rayleigh number in a pure-CO₂ system.

DOI: [10.1103/PhysRevFluids.7.114501](https://doi.org/10.1103/PhysRevFluids.7.114501)

I. INTRODUCTION

In the last several decades, humans have suffered from more and more serious climate problems, such as reduction of average rainfall, extreme heat waves, and unexpected droughts or floods, which have been identified as likely outcomes of global warming [1]. Among greenhouse gases which are the leading causes of global warming, carbon dioxide (CO₂) is the most significant among all greenhouse gases for efficient climate control due to its large percentage [1–3]. Therefore, how to reduce CO₂ in the atmosphere has become an essential requirement for remediation [4]. To date, many efforts have been made, including the development and utilization of clean energy [4] and the storage of CO₂ [5,6]. In terms of storage of CO₂, sequestration of CO₂ in deep saline aquifers has been identified as the most feasible solution to the problem due to its extended storage capacity,

*Corresponding author: zlguo@hust.edu.cn

proximity to emission sources, and worldwide availability [7,8]. After injection, CO₂ spreads under the barrier of the low-permeability cap rocks in a supercritical state due to the buoyancy and gradually dissolves into the saline brine forming a denser diffusive layer. This density stratification may lead to a density-driven instability [9,10], which increases the rate of mass transport from the supercritical state into the brine, and reduces the risk of leakage. In addition, it should be noted that certain impurities such as N₂, O₂, Ar, and CH₄ may also be co-injected in geological storage due to the high cost of the separation of CO₂ from gas streams [11,12]. Gases such as H₂S and SO₂ may be intentionally co-injected to be disposed of [13] due to their detriment to the environment. Although the amount of impurity gases is relatively small in injected gas compositions, due to their influence of compressibility on the transportation, some impurities such as H₂S, SO₂, and N₂ take up a considerable portion in the dissolved gas compositions because of their higher solubility compared to CO₂ [14]. These impurities are different from CO₂ chemically and physically, which could influence the convective mixing process and thus affect the security of the storage. For example, SO₂ was proven to increase the density of the brine, which would enhance the density-driven convective mixing process [14,15], while H₂S and N₂ were implied to have negative effects on the density of aqueous solution compared with CO₂ and SO₂, which could bring inhibitive effects for the density-driven instability [11,16]. Due to their important roles in the dissolution trapping mechanism, the effect of the co-injected impurities should be considered in the design and operation of geological storage of CO₂.

Compared with the extensive research on pure CO₂ [17–20], few studies focus on the convective mixing process in brine sequestration of impure CO₂. Among them, Wang *et al.* [21] theoretically investigated the effects of the impure CO₂, and they found that the impurities have important impacts on CO₂ storage capacity, storage integrity, and injectivity. Li *et al.* [22,23] performed nonlinear numerical simulations to investigate the effects of the N₂ and SO₂ impurities on the dissolution trapping mechanism of CO₂ storage; they thought that N₂ could delay the onset of convection and reduce the dissolution rate and the storage capacity, while some impurities such as SO₂ are implied to enhance the solubility trapping mechanism. However, although the above research has yielded some meaningful results, an important physical mechanism, namely, double diffusive effects due to the different molecular diffusion of the CO₂ and impurities, has been ignored in these studies. In fact, such a difference could bring about a nonmonotonic density profile in the dissolution process, leading to a quite different instability pattern compared with the CO₂-brine system. In view of this important mechanism, Jafari Raad *et al.* [24] conducted a linear stability analysis to investigate the effect of impurity in CO₂ streams on the convective mixing associated with the sequestration of impure CO₂ in deep saline aquifers. They drew a conclusion that H₂S has a potential to accelerate the onset of density-driven instabilities, which could lead to more effective solubility trapping. The dissolution of H₂S could reduce the density of brine, thus reducing the driving force of the convection mixing process. So it is generally believed that H₂S should impede the buoyancy-driven instabilities resulting in less efficient CO₂ solubility trapping previously. The work of Jafari Raad showed the contrasting conclusion to the original idea. However, Kim *et al.* [12] disputed this conclusion in their subsequent work. They conducted that for a given Rayleigh number (Ra), the dissolution of N₂ and H₂S impurities makes the system stable, whereas dissolved SO₂ accelerates the onset of instability through theoretical and numerical analysis. The dispute over this problem has still not been resolved. Mahmoodpour and coworkers [25–27] performed a series of studies to investigate the effects of impurities, including N₂ and SO₂, on the dissolution convection processes. They found that impurities could influence the diffusion coefficient of CO₂ in brine, and further influence the convection mixing processes of the system. N₂ impurity could show higher dissolution flux at early time as compared to those with pure CO₂. So far, the investigations into the impacts of impurities on the convective mixing process are ongoing and still controversial, so the topic is still worth studying. In particular, all the relative studies mentioned above were performed at representative elementary volume (REV) scale, where a number of assumptions are required. Tartakovsky *et al.* [28] have argued that the REV-scale flow and transport model tends to overpredict the degree of mixing, which has a significant impact on the prediction of the nonlinear convective

mixing process. Therefore, a detailed study of multicomponent convective mixing process and characterization of the transport phenomenon of CO₂ plumes at pore scale is still necessary.

In addition, it has been widely accepted that in the single-component system, such as pure CO₂ sequestration, the onset time of gravitational instability versus the logarithm of the Ra has a linear relation with a slope of -2 . However, this relation has not been shown in the multicomponent system. In order to investigate the instability scaling relations in multicomponent systems, Jafari Raad *et al.* [24] and Kim *et al.* [12] have done some research in previous work but have not given a reasonable result. Recently, Mahmoodpour *et al.* [25] experimentally determined the effect of the impurity N₂ on the convective dissolution of CO₂. Based on their experiments, they insist that the same scaling relation in the single-component system can be used in the multicomponent system when the effective diffusivity is used in the definition of Ra. However, the effective diffusion coefficient values should be calculated through experimental data in their study, which is not intuitive. Later Jafari Raad *et al.* [29] suggested similar scaling relations for part of the parameter regions by using the maximum density difference as a proper scaling parameter. In their work, the maximum density difference can be calculated according to the density distribution of the system. In a subsequent work, Kim *et al.* [30] tried to find the scaling relations in the other regions. The temporal change of the density gradient is suggested as the new scaling parameter rather than the density difference used in the study of Jafari Raad [29], and the proper scaling relations were obtained based on their linear stability results. It is obvious that the scaling relations of the stability of impure systems have attracted much attention, but some limitations for the current research still exist. First, the scaling relations for the region, where the impurity SO₂ is located, are still lacking. Li *et al.* [14] found that the effects of other common impurities seem unlikely to make much difference on CO₂ diffusivity, but the existence of SO₂ is supposed to influence the practical CO₂ diffusivity. Therefore, it seems necessary to perform more reasonable predictions of scaling relations when SO₂ is involved. Second, the mathematical form of the scaling relations proposed by Kim *et al.* [30] is not uniform in different regions, including scaling parameter and scaling order, which makes it difficult to compare different systems in different regions. Third, the above scaling relations are all obtained through the quasi-steady-state approximation (QSSA) method, which is a method of linear stability analysis. Despite the fact that the QSSA method predicts that perturbations become linearly unstable at a limited critical time $t = t_c$, it predicts wildly different results for t_c depending on the growth norm chosen [31], which may lead to inexactitude of scaling relations. Finally, the exiting studies often focus on the critical time t_c for linear instability, but the onset time t_{on} is arguably more important than t_c when evaluating sequestration sites, because t_{on} marks the time when nonlinear mechanisms cause an increase in the rate of CO₂ dissolution. In summary, there is still a lack of a unified mathematical scaling relation for t_{on} in impure systems.

In this paper, an investigation into the convective mixing process in brine sequestration of impure CO₂ is performed from a pore-scale perspective. The convective mixing process in different intervals is analyzed in detail, and based on the numerical results at pore scale, the effective Rayleigh number Ra_e in the full parameter range of the impure system is obtained, where the scaling relations between Ra_e and the onset time of convection are consistent with the single-component system. The rest of the paper is organized as follows. Section II and Sec. III introduce the governing equation and numerical method at pore scale, respectively. Section IV presents the results from the pore-scale LBM simulations, followed by conclusions in Sec. V.

II. PROBLEM FORMULATION

A. Model description

In the present study, two-dimensional isotropic synthetic porous media generated with a staggered array of uniform circular grains as displayed in Fig. 1 is considered. The typical parameters including formation and simulation parameters are listed in Table I.

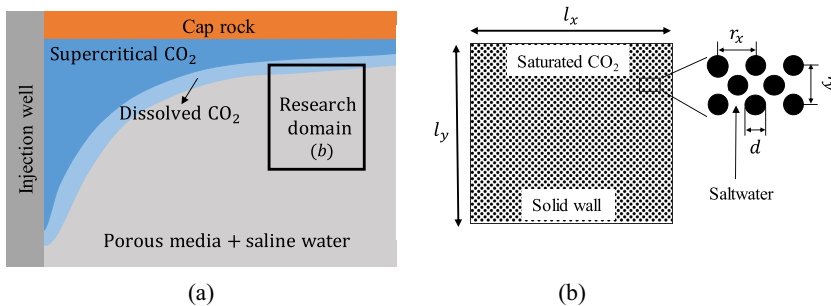


FIG. 1. Schematic of the model domain for the solubility trapping mechanism. (a) Domain representation and (b) computational configuration.

Previous studies showed that the interface between CO₂ and brine is almost not deflected by the underlying convection, and this immiscible convective mixing process can be simplified to a single-phase problem, with the phase interface between CO₂ and brine being represented by a fixed impervious top boundary [17,33]. Under the above assumption, the upper boundary is considered to be sharp with constant concentration of CO₂ and impurities. As shown in Fig. 1, it can be regarded as an interface beneath the phase interface, which is filled with saturated CO₂ and impurities. The bottom of the computational domain is set as an impermeable boundary to represent the impermeable rocks, and the periodic boundary condition is adopted at the lateral boundaries. Initially, the porous medium is filled with the brine and fluid with saturated CO₂ and impurities is placed above the region and continuously diffused into the computational domain. Over time, the upper solutes gradually diffuse into the host fluid causing density instability. In this paper, we express the impurity as b for convenience, and the effects of different impurities on the system are studied by changing the relevant parameters, such as the density expansion coefficient and molecular diffusion coefficient. CO₂ is written as a for simplicity of expression. In addition, thermal effects are neglected and the geochemical reactions are not taken into account in this study; these will be studied particularly in our future work.

B. Governing equations

The fluid motion and the transport of CO₂ and impurities in this process can be described by the incompressible Navier-Stokes (NS) equations and the convection-diffusion (CD) equations,

$$\nabla \cdot \mathbf{u} = 0, \quad (1a)$$

$$\rho_0 \left(\frac{\partial \mathbf{u}}{\partial t} + \mathbf{u} \cdot \nabla \mathbf{u} \right) = -\nabla p + \nabla \cdot (\nu \rho_0 \nabla \mathbf{u}) + \rho(C)g\mathbf{j}, \quad (1b)$$

TABLE I. Fluid properties [32].

Variables	Realistic values	Simulated values (lattice unit)
Viscosity, μ	0.5947×10^{-3} Pa s	1.5×10^{-4}
Density of fluid, ρ_w	994.56 kg m ⁻³	1
Density increase due to CO ₂ , $\Delta\rho/\rho$	0.5%	0.5%
CO ₂ diffusivity, D	2×10^{-9} m ² s ⁻¹	5×10^{-6}
Gravitational acceleration, g	9.81 m/s ²	9.81
Domain width, l_x	129.8 mm	1.125
Domain height, l_y	115.4 mm	1

$$\frac{\partial C_a}{\partial t} + \mathbf{u} \cdot \nabla C_a = D_a \nabla^2 C_a, \quad (1c)$$

$$\frac{\partial C_b}{\partial t} + \mathbf{u} \cdot \nabla C_b = D_b \nabla^2 C_b, \quad (1d)$$

where $\mathbf{u} = (u, v)$ is the velocity, p is the pressure, ν is the fluid viscosity, g is the gravity, \mathbf{j} is the unit vector in the direction of gravity, D_i is the diffusion coefficient, and C_i represents the concentration of component i , where $i = a, b$ represents different species. In our present work, the diffusion coefficient of CO₂, i.e., D_a is assumed constant, and no cross-diffusion is considered. In addition, the flow of the fluid is incompressible. With the Boussinesq approximation, the density ρ is considered as constant except in the body-force term, where it is assumed to depend linearly on the concentration C_i ,

$$\rho(C) = \rho_0(1 + \beta_a C_a + \beta_b C_b), \quad (2)$$

where β_i is the concentration expansion coefficient.

In order to trigger density instability, a small perturbation $\varepsilon(x)$ is introduced in the initial concentration of CO₂,

$$\varepsilon(x) = \left\{ \sum_m [a_m \cos(k_m x) + b_m \sin(k_m x)] \right\} / m, \quad (3)$$

where m is the wave number of the perturbation, $k_m = 2m\pi/l_x$ is the perturbation frequency, and a_m and b_m are random numbers in accordance with the Gaussian distribution with the range of 0%–0.1%, which represents the perturbation amplitude. In order to avoid negative concentration, the concentration of the host fluid at the top layer is initialized as $-\varepsilon_{\min} + \varepsilon(x)$ where ε_{\min} is the minimum value of $\varepsilon(x)$. After the robustness of the results for different initial noises was validated, the same set of noises are used throughout all testing cases to prevent the effects of various initial perturbations on the numerical results.

The boundary conditions for this problem can be described as

$$\begin{aligned} C_a(0, y, t) &= C_a(l_x, y, t), & C_b(0, y, t) &= C_b(l_x, y, t), & \mathbf{u}(0, y, t) &= \mathbf{u}(l_x, y, t), \\ \nabla C_a(x, 0, t) &= (0, 0), & \nabla C_b(x, 0, t) &= (0, 0), & \mathbf{u}(x, 0, t) &= (0, 0), \\ C_a(x, l_y, t) &= C_{a0}, & \nabla C_b(x, l_y, t) &= C_{b0}, & \mathbf{u}(x, 0, t) &= (0, 0), \end{aligned} \quad (4)$$

where C_{a0} and C_{b0} are the saturated concentration of CO₂ and impurities. For the sake of easier analysis, Eqs. (1) can be expressed in a dimensionless form by introducing the following characteristic variables:

$$L = l_y, \quad U = \sqrt{g\beta_a L C_{a0}}, \quad T = L/U, \quad C_1 = C_{a0}, \quad C_2 = C_{b0}. \quad (5)$$

With the nondimensional variables

$$\mathbf{u}^* = \frac{\mathbf{u}}{U}, \quad \mathbf{x}^* = \frac{\mathbf{x}}{L}, \quad C_a^* = \frac{C_a}{C_1}, \quad C_b^* = \frac{C_b}{C_2}, \quad t^* = \frac{t}{T}, \quad p^* = \frac{p}{\rho_0 U^2} + \frac{gL_y}{U^2}, \quad (6)$$

the dimensionless form of Eqs. (6)–(9) can be expressed as

$$\nabla \cdot \mathbf{u}^* = 0, \quad (7)$$

$$\frac{\partial \mathbf{u}^*}{\partial t^*} + \mathbf{u}^* \cdot \nabla \mathbf{u}^* = -\nabla p^* + \sqrt{\frac{\text{Sc}}{\text{Ra}}} \nabla \cdot (\nabla \mathbf{u}^*) + (C_a^* + R_\beta R_C C_b^*) \mathbf{g} \mathbf{j}, \quad (8)$$

$$\frac{\partial C_a^*}{\partial t^*} + \mathbf{u}^* \cdot \nabla C_a^* = \frac{1}{\sqrt{\text{RaSc}}} \nabla^2 C_a^*, \quad (9)$$

$$\frac{\partial C_b^*}{\partial t^*} + \mathbf{u}^* \cdot \nabla C_b^* = \frac{R_D}{\sqrt{\text{RaSc}}} \nabla^2 C_b^*, \quad (10)$$

where the variables with an asterisk are the corresponding dimensionless ones, $R_\beta = \beta_b/\beta_a$ is the ratio of the coefficients of density variation of impurities to CO_2 . $R_C = C_2/C_1$ and $R_D = D_b/D_a$ are the ratio of the saturated concentration and diffusion coefficient of species in the aqueous phase, respectively. Ra and Sc are the dimensionless Rayleigh number and Schmidt number, respectively, which can be expressed as

$$\text{Ra} = \frac{L^3 g \beta_a C_1}{\nu D_a}, \quad \text{Sc} = \frac{\nu}{D_a}. \quad (11)$$

The behaviors of the density-driven convective mixing process with impure CO_2 can be characterized by all these dimensionless numbers.

III. NUMERICAL METHOD

In this work the multiple-relaxation time (MRT) lattice Boltzmann equation (LBE) [34,35] is employed to solve the above governing equations, which can improve the stability of calculation and avoid the unphysical dependence of permeability on viscosity for simulation. Specifically, the most popular two-dimensional nine-velocity (D2Q9) LB model is employed to solve the fluid flow. The evolution equation for the incompressible NS equations is written as

$$\mathbf{f}(\mathbf{x} + \mathbf{c}_i \delta_t, t + \delta_t) - \mathbf{f}(\mathbf{x}, t) = -(\mathbf{M}^{-1} \mathbf{S})[\mathbf{m}(\mathbf{x}, t) - \mathbf{m}^{\text{eq}}(\mathbf{x}, t)] + \mathbf{M}^{-1} \delta_t \hat{\mathbf{F}}, \quad (12)$$

where \mathbf{f} is the density distribution function, δ_t is the time step, and \mathbf{c}_i is the discrete lattice velocity. \mathbf{M} is the transformation matrix, $\mathbf{S} = \text{diag}[s_0, \dots, s_8]$ is the diagonal relaxation factor matrix, \mathbf{m} is the moments at moment space, and \mathbf{m}^{eq} denotes the equilibrium distribution functions at the moment space. To reduce the compressible effect, the He-Luo incompressible model [36] is employed, and the equilibrium PDF reads

$$f_i^{\text{eq}}(x, y, t) = \omega_i \left[\rho + \frac{\mathbf{c}_i \cdot \mathbf{u}}{c_s^2} + \frac{(\mathbf{c}_i \cdot \mathbf{u})^2}{2c_s^4} - \frac{u^2}{c_s^2} \right], \quad (13)$$

where $c_s = c/\sqrt{3}$ is the lattice sound speed with $c = \delta_x/\delta_t$ being the lattice speed. The corresponding equilibrium distribution functions at the moment space \mathbf{m}^{eq} can be expressed as

$$\begin{aligned} \mathbf{m}^{\text{eq}} &= \mathbf{M} \cdot \mathbf{f}^{\text{eq}} = (0, e, \epsilon, j_x, q_x, j_y, q_y, p_{xx}, p_{xy})^T \\ &= (0, -2\rho + 3u^2, \rho - 3u^2, u, -u, v, -v, u^2 - v^2, uv)^T. \end{aligned} \quad (14)$$

In addition, $\hat{\mathbf{F}}$ in Eq. (12) represents the discrete external force in moment space, which can be expressed as

$$\hat{\mathbf{F}} = (\mathbf{I} - \mathbf{S}/2)\mathbf{M}\bar{\mathbf{F}}. \quad (15)$$

To avoid the discrete lattice effects, a representation of the forcing term proposed by Guo *et al.* [37] is employed for the external force \mathbf{F} , which can be expressed as

$$\bar{\mathbf{F}}_i = \omega_i \left[\frac{\mathbf{c}_i \cdot \mathbf{F}}{c_s^2} + \frac{\mathbf{u}\mathbf{F} : (\mathbf{c}_i \mathbf{c}_i - c_s^2 \mathbf{I})}{c_s^4} \right]. \quad (16)$$

The fluid density and velocity in the present model can be calculated as

$$\rho = \sum_0^8 f_i(\mathbf{x}, t), \quad \mathbf{u} = \sum_1^8 c_i f_i(\mathbf{x}, t) + \frac{\delta_t \mathbf{F}}{2}. \quad (17)$$

It should be noted that Eq. (12) can be recovered to NS equations through Chapman-Enskog expansion analysis with

$$\nu = c_s^2 \left(\tau_\nu - \frac{1}{2} \right) \delta_t, \quad (18)$$

where $\tau_\nu = 1/s_7 = 1/s_8$ is the viscosity related relaxation time.

In addition, the two-dimensional five-velocity (D2Q5) model [38] is employed to solve the solutes transport, which could reduce the computational cost without loss of accuracy. The evolution equation for CD equation can be expressed as [38]

$$\mathbf{g}(\mathbf{x} + \mathbf{c}_i \delta_t, t + \delta_t) - \mathbf{g}(\mathbf{x}, t) = -(\mathbf{M}'^{-1} \mathbf{S}') [\mathbf{n}(\mathbf{x}, t) - \mathbf{n}^{\text{eq}}(\mathbf{x}, t)], \quad (19)$$

where \mathbf{g} denotes the particle distribution function, $\mathbf{S}' = \text{diag}[s'_0, \dots, s'_8]$ is the diagonal relaxation factor matrix in moment space, \mathbf{n} is the moments at moment space, and \mathbf{n}^{eq} denotes the corresponding equilibrium distribution functions at the moment space, which is expressed as

$$\mathbf{n}^{\text{eq}} = C \left(1, 0, 0, -\frac{2}{3}, 0 \right)^T. \quad (20)$$

The concentration of a species C can be calculated by

$$C = \sum_{i=0}^4 g_i. \quad (21)$$

The diffusion coefficient is determined by

$$D = c_s^2 \left(1/s'_1 - \frac{1}{2} \right) \delta_t = c_s^2 \left(1/s'_2 - \frac{1}{2} \right) \delta_t, \quad (22)$$

During the numerical simulations, the no-slip velocity and prescribed concentrations at top boundary and impermeable concentration conditions at bottom boundary are realized by the exact nonequilibrium extrapolation boundary scheme [39]. The no-slip and impermeable concentration conditions at the porous matrix interface are treated with the bounce-back scheme.

IV. RESULTS AND DISCUSSION

A. Density distribution in differential diffusion system

Dissolution of CO_2 in brine could slightly increase the density of the aqueous phase, which creates a precondition for gravitational instability. However, the presence of impurities may alter the density distribution, affect the convective mixing process, and then influence the efficiency of storage. It is necessary to analyze density distribution in differential diffusion systems before the onset of the convection.

Initially, the spreading of the species is driven by diffusion, and the governing equations for this dissolution process are Eqs. (1c) and (1d) with the velocity stagnant, which can be expressed as

$$\frac{\partial C_i}{\partial t} = D_i \frac{\partial^2 C_i}{\partial y^2}. \quad (23)$$

In addition, prior to the onset of convection, the thickness of the diffusive layer is narrow enough compared with the domain layer thickness L . With the initial and boundary conditions described above, the analytical solution for Eq. (23) can be expressed as [24]

$$C_i(y, t) = C_{i0} \text{erfc}(y/\sqrt{4D_i t}). \quad (24)$$

Combing Eq. (2) and Eq. (24), the density distribution of the system can be written as

$$\begin{aligned}\rho(C, t) &= \rho_0 \beta_a C_{a0} (1 + C_a^* + R_\beta R_C C_b^*) = \rho_0 \beta_a C_{a0} (1 + \rho^*) \\ &= \rho_0 \beta_a C_{a0} [1 + \operatorname{erfc}(y/\sqrt{4D_a t}) + R_\beta R_C \operatorname{erfc}(y/\sqrt{4D_b t})],\end{aligned}\quad (25)$$

where ρ^* is the dimensionless density corresponding to the body-force term. It can be seen from Eq. (25) that the analytical expression of density is a one-dimensional solution, due to the adoption of periodic boundary conditions for the left and right boundaries. Further, in order to obtain the space distribution of the density clearly, the spatial derivative of the density is calculated, which can be expressed as

$$\frac{\partial \rho}{\partial y} = -\frac{\rho_0 \beta_a C_{a0}}{\sqrt{D_a \pi t}} \left[\exp\left(-\frac{y^2}{4D_a t}\right) + \frac{R_\beta R_C}{\sqrt{R_D}} \exp\left(-\frac{y^2}{4D_b t}\right) \right]. \quad (26)$$

According to Eq. (26), the different density profile with depth can be specified.

First, when the density profile decreases monotonically along the direction of gravity, the derivative of density satisfies $\partial \rho / \partial y < 0$. According to Eq. (26), we can obtain

$$-\frac{R_\beta R_C}{\sqrt{R_D}} \exp\left(-\frac{y^2}{4R_D D_a t}\right) < \exp\left(-\frac{y^2}{4D_a t}\right). \quad (27)$$

Obviously, the above formula always holds when $R_\beta R_C \geq 0$. When $R_\beta R_C < 0$, Eq. (27) can be further simplified by taking natural logarithm at the left- and right-hand sides of the equation:

$$\ln\left(-\frac{R_\beta R_C}{\sqrt{R_D}}\right) < \left(\frac{1}{R_D} - 1\right) \frac{y^2}{4D_a t}. \quad (28)$$

When $-R_\beta R_C < \sqrt{R_D}$, $\ln(R_\beta R_C / \sqrt{R_D}) < 0$. However, when $R_D < 1$, the right-hand side of the equation (28) is greater than zero. In this condition, Eq. (28) always holds. In summary, the density profile decreases monotonically when $R_\beta R_C > 0$ or $-R_\beta R_C < \sqrt{R_D}$ coupled with $R_D < 1$.

When $\partial \rho / \partial y > 0$, the density profile increases monotonically. Similarly, according to Eq. (26), we can obtain

$$\ln\left(-\frac{R_\beta R_C}{\sqrt{R_D}}\right) > \left(\frac{1}{R_D} - 1\right) \frac{y^2}{4D_a t}. \quad (29)$$

When $-R_\beta R_C > \sqrt{R_D}$, $\ln(R_\beta R_C / \sqrt{R_D}) > 0$. Equation (29) always holds when the right side of Eq. (29) is less than zero, i.e., $R_D > 1$. In summary, the density profile increases monotonically when $-R_\beta R_C > \sqrt{R_D}$ coupled with $R_D > 1$.

Finally, the cases with nonmonotonic density are considered. In this condition, the density profiles have extremum (local minimum or maximum). By setting $\partial \rho / \partial y = 0$, and taking the natural logarithm of the expression, we can obtain

$$\frac{(1 - R_D)}{4D_b t} y^2 - \ln\left(-\frac{R_\beta R_C}{\sqrt{R_D}}\right) = 0. \quad (30)$$

The discriminant of the above quadratic equation can be expressed as

$$\Delta = \frac{(1 - R_D)}{D_b t} \ln\left(-\frac{R_\beta R_C}{\sqrt{R_D}}\right). \quad (31)$$

The condition for the existence of solution of Eq. (30) is $\Delta \geq 0$. According to Eq. (31), we can obtain that when $-R_\beta R_C \geq R_D^{1/2}$ with $R_D \leq 1$ or $-R_\beta R_C \leq R_D^{1/2}$ with $R_D \geq 1$, $\Delta \geq 0$. Further, with the help of the gradient of density near the top boundary, the behavior of the density profile with depth can be inspected.

In addition, according to the second derivative of density, the critical curve of the density profile with an inflection point can be expressed as $R_D = (-R_\beta R_C)^{2/3}$. Figure 2 shows a summary of the

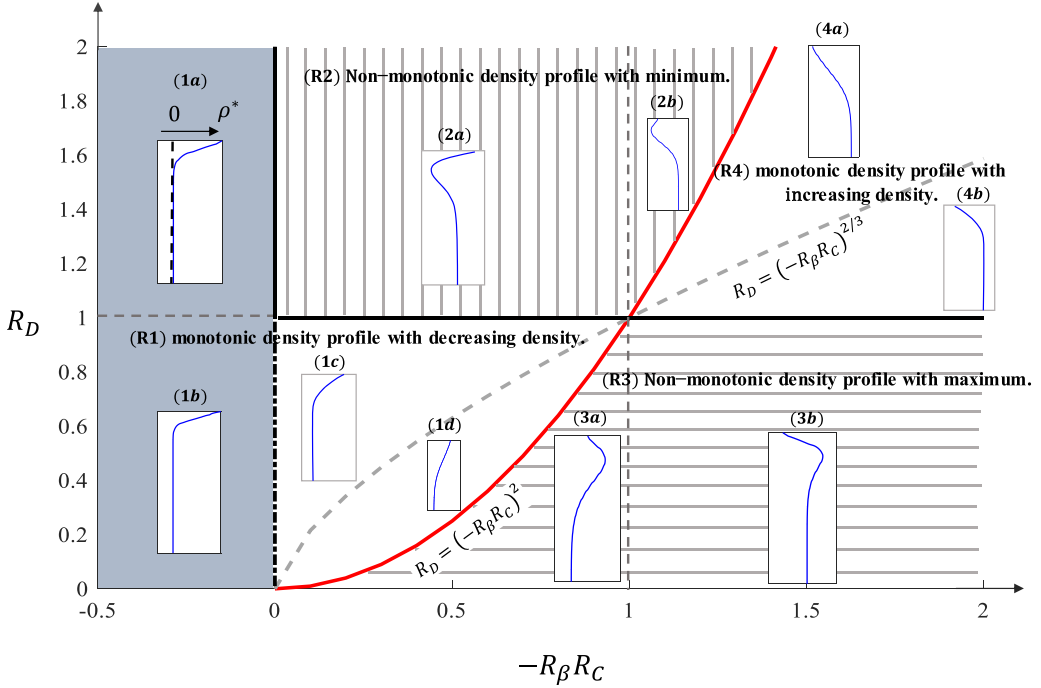


FIG. 2. Classification of parameter space $(-R_\beta R_C, R_D)$ based on the different density distribution.

different regions in the parameter space $(-R_\beta R_C, R_D)$ based on the different density profile. Four basic regions can be classified, including regions with nonmonotonic and monotonic density profiles. Actually, such convective mixing processes in systems with nonmonotonic density distributions are common in reactive dissolution process [40,41]. For example, Jotkar *et al.* [41] investigated the impact of differential diffusion on such reactive convective dissolution in the nonlinear regime numerically. They specifically determined how the ratio of the diffusion coefficients affects the temporal evolution of the dissolution flow, its asymptotic value, and the moment at which convection begins. However, the chemical reactions play important roles in their study which are not considered in the present study.

B. Nonlinear simulations for each region

In this section the nonlinear numerical simulations for density-driven convective mixing processes with different components are presented. The present work focuses on the influences of the impurities, thus the Rayleigh number is fixed as $Ra = 4 \times 10^8$, and in order to achieve the accuracy and stability of the calculation, a smaller Schmidt number, $Sc = 10$, was taken to calculate the convective mixing processes referring to the treatments in existing works [20,42], which might change the relative thickness of the momentum and solute diffusive boundary layers, but the calculation results are still referential. Different $R_\beta R_C$ and R_D are selected to investigate the influences of different impurities. The diffusion coefficient of CO_2 is fixed as $D_a = 1 \times 10^{-6}$, and other relevant parameters are set as

$$\begin{aligned}
 L = 1, \quad C_1 = 1, \quad U = \frac{D_a}{L} \sqrt{RaSc}, \quad T = \frac{L}{U}, \quad D_b = D_a R_D, \\
 v = Sc D_a, \quad \tau_v = \frac{v}{c_s^2 \delta_t} + \frac{1}{2}, \quad \tau_{D_a} = \frac{D_a}{c_s^2 \delta_t} + \frac{1}{2}, \quad \tau_{D_b} = \left(\tau_{D_a} - \frac{1}{2} \right) R_D + \frac{1}{2}.
 \end{aligned} \tag{32}$$

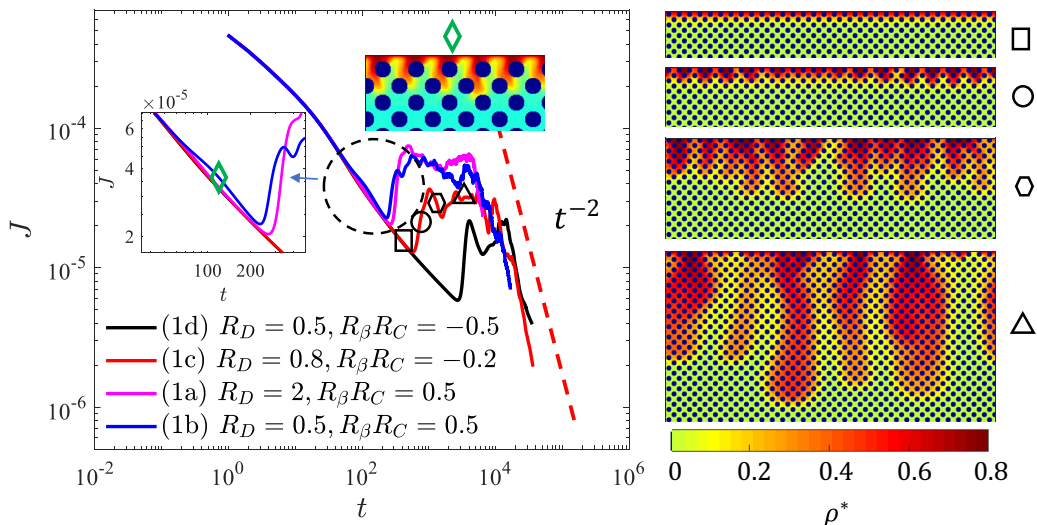


FIG. 3. Temporal dynamics of horizontally averaged dissolution flux J with different $R_\beta R_C$ and R_D in region R1.

In addition, a mesh of size $N_x \times N_y = 1152 \times 1024$ is chosen for the subsequent simulations, with the grid convergence tests being carried in our previous study [43]. The diameter of the grain is set as $d = 18\delta_x$. The closest center-to-center distance between two cylinders in the x and y directions is $r_x = r_y = 36\delta_x$. The porosity of the porous network is about 0.57, and the permeability of this structure is about 2.87×10^{-6} . In the following, the general phenomena of convective mixing processes are investigated.

Cases R1: Simulations are first conducted for region R1. As in the above analysis, the density profiles are monotone decreasing in this region, and the density instability could be induced in all cases. Since the density profile also decreases monotonically in the absence of impurities, the general fingering characteristics in this region should be consistent with those of a pure CO_2 system. As displayed in Fig. 3, the dissolution flux of CO_2 with different impurities goes through several similar stages including the diffusion-dominated regime, flux-growth regime, merging regime, constant flux regime, and shutdown regime. However, although different flux profiles are consistent in trend, the onset time, which is defined as the turning point of the diffusion-dominated regime to the flux growth regime, are influenced by $-R_\beta R_C$ and R_D . Moreover, as marked in Fig. 3, the denser fluid begins to generate tiny fingers in the space between circular grains when $R_D = 0.5$, $R_\beta R_C = 0.5$, which causes the fluctuation of the flux in the diffusion-dominated regime. According to our previous study [43], this phenomenon usually occurs at high Rayleigh numbers. It means that the influence of impurities on the system can be approximately equivalent to the influence of Ra , and there is an effective Rayleigh number Ra_e which could contain the influence of parameters $R_D = 0.5$, $R_\beta R_C = 0.5$. Here the general phenomena in each region are introduced only, and the definition of Ra_e will be discussed in detail in the next section.

Cases R2: In this region, impurities have opposite effects on the density of the saline solution compared with CO_2 , and the diffusion rate of CO_2 is also less than that of impurities. Under the joint action, the density could form a layered structure along the depth before instability. As shown in Fig. 4, the less dense layer L2, which is formed due to the rapid diffusion of impurities, is sandwiched between the denser layers L1 and L3. Since the miscible interface above the lower density layer is more likely to be unstable, therefore the instability will be induced at L1. In addition, according to the relative magnitude of the density of L1 and L3, region R2 can be further divided

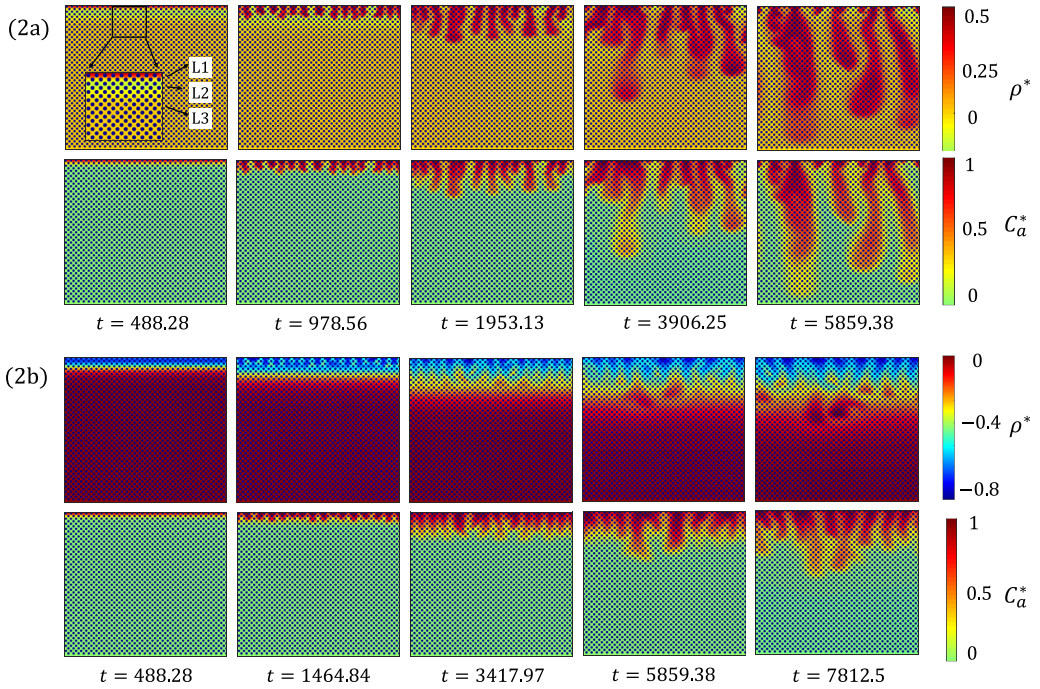


FIG. 4. Snapshots of the solute concentration profile in region R2, (2a) $R_D = 5$, $R_\beta R_C = -0.5$, (2b) $R_D = 5$, $R_\beta R_C = -1.7$.

into (2a) and (2b) with $1 + R_\beta R_C > 0$ and $1 + R_\beta R_C < 0$, respectively, and the time evolution of the convective mixing processes in these two subregions is investigated. Two groups of parameters with $R_D = 5$, $R_\beta R_C = -0.5$, and $R_D = 5$, $R_\beta R_C = -1.7$ are selected to display the different phenomena.

When $1 + R_\beta R_C > 0$, as shown in Fig. 4(a), after the initial diffusion, some tiny fingers develop and sink from the top layer L1 toward the less dense layer L2. In addition, since the density of L1 is greater than that of L3, the fingers could easily develop and travel from L2 to L3, destroying the stratification of the density and creating a global convection. A similar conclusion can be drawn from the analysis of the horizontal-average density profile at different time. As shown in Fig. 5, the density profile has a clear three-layer structure at the early time, i.e., the diffusive denser layer L1, the less dense layer L2, and the host fluid L3, and there is a minimum of the horizontally averaged density profile at L2 in this initial stage. As time goes on, the density minimum disappears, and the convection is driven by the difference between the top diffusive layer and bottom saline water, which is consistent with the convective mixing process of pure CO_2 . Therefore, the development and interaction between fingers are basically the same as those without impurities, which can be identified in Fig. 4(a).

Fingering phenomena with $1 + R_\beta R_C < 0$ are shown in Fig. 4(b). The instability also occurs at the top layer, and then the tiny fingers develop. However, in this scenario, the densities of L1 and L2 are all smaller than that of L3, so the bottom layer can act as an inhibiting barrier to hinder fingering progression. In the early stage of convection, the fingers are so weak that they cannot break through the barrier of L3, where the dense fingers are limited. It can be seen that, due to limitation of the convection, fingers are short and numerous. The interactions are also reduced due to the weak convection, and the enhancement effect of convection on solute transport is greatly weakened. However, convection is not always confined to a finite space at the top layer. As shown in Fig. 5(b), different from the cases with $1 + R_\beta R_C > 0$, the horizontally averaged density profile will always have a minimum value at any stage of development. It means that despite the suppression of L3, the

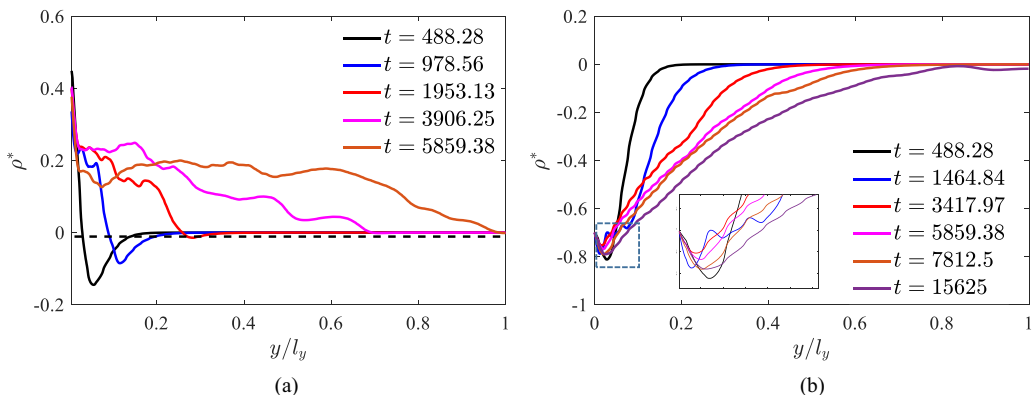


FIG. 5. Time evolution of horizontally averaged density profile: (a) $R_D = 5, R_\beta R_C = -0.5$, (b) $R_D = 5, R_\beta R_C = -1.7$.

system is still in an unstable state and could not form a stable stratification. As shown in Fig. 6(b), when a local finger carries a large amount of dense fluid due to the merging with neighboring fingers, its downward inertia allows it to break through the barrier and perturb the interface between L2 and L3. However, it is difficult for these fingers to trigger global convection, which would be cut by the interface of L3, leaving a neat group of fingers. The broken part will move and diffuse in L3 like isolated drops until it dies out. With time moving on, the boundary between L3 and L2 becomes blurred due to the influence of convection and diffusion. It can be seen in Fig. 5(b), L3, which is defined as the layer with the density of the host fluid, is gradually squeezed. The fingers front could gradually develop downward with the migration of the interface between L2 and L3.

The time evolution of dissolution flux of CO_2 at the top boundary is also investigated in R2. Figure 6(a) shows the profiles of the flux with different $R_\beta R_C$. It can be seen that, with the decreasing $R_\beta R_C$, the merging regimes take longer. This is because the defensive effect of L3 becomes stronger with the decrease of $R_\beta R_C$, which weakens the interactions of fingers. On the other hand, in the constant flux regime, some small fingers on the boundary layer are reinitiated, and most of them are swept into the existing plumes, which provides the driving force for the continued development

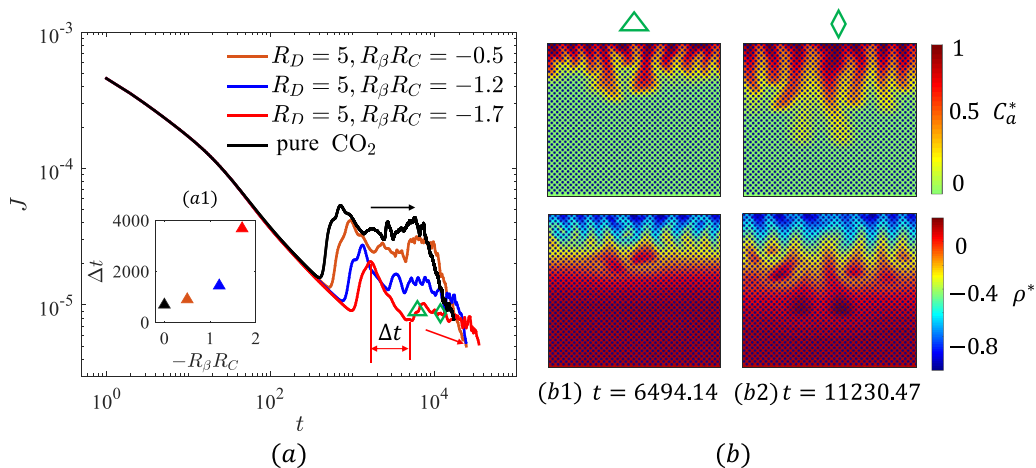


FIG. 6. Temporal dynamics of horizontally averaged dissolution flux J with different $R_\beta R_C$ and R_D in region R2.

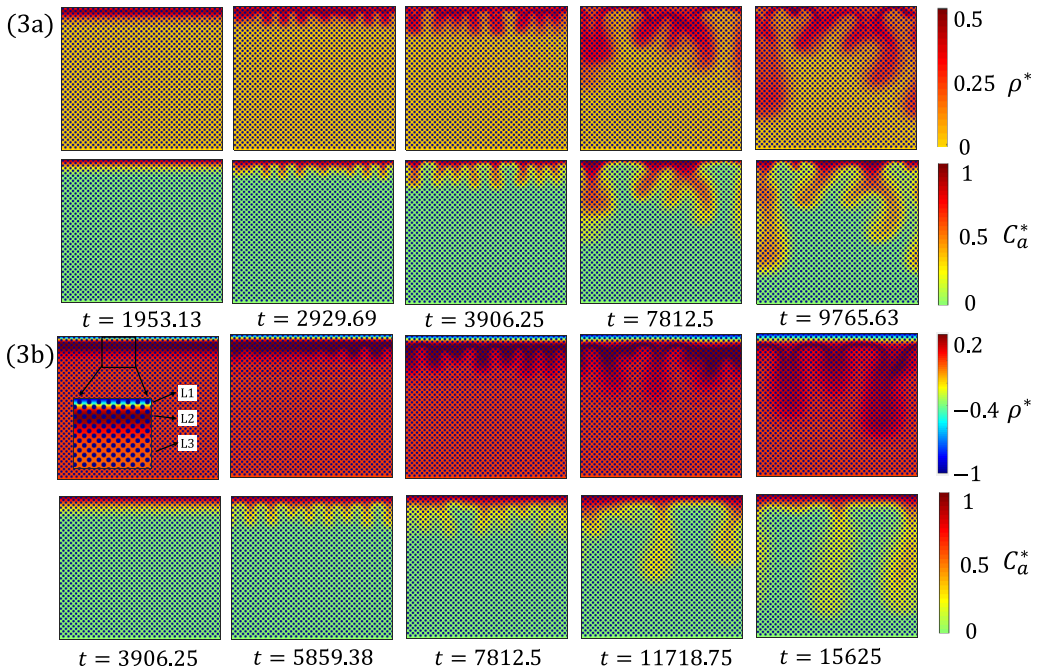


FIG. 7. Snapshots of the solute concentration profile in region R3, (3a) $R_D = 0.2$, $R_\beta R_C = -0.8$, (3b) $R_D = 0.2$, $R_\beta R_C = -2$.

of the plume. In this process, the dissolution flux can be regarded as constant approximately due to the equilibrium of development of plumes and reinitiations. However, the appearance of L3 inhibits the intensity of convection, leading to the disappearance of equilibrium at this stage. As shown in Fig. 6(a), as $R_\beta R_C$ decreases, the flux declines obviously after the merging regime, which makes a significantly difference from pure CO_2 system.

Cases R3: Fingering phenomena in region R3 are then simulated. Due to the differences of the diffusion coefficient and the concentration expansion coefficient, a density stratification can also be generated, including a less dense fluid layer L1, a dense layer L2, and a host fluid layer L3. As displayed in Fig. 7, L2 is a layer with local maximum density, where the instability will be induced. Similarly, according to the relative magnitude of the density of L1 and L3, region R3 is divided into (3a) and (3b) with $1 + R_\beta R_C > 0$ and $1 + R_\beta R_C < 0$. Time evolution of density and concentration with $R_D = 0.2$, $R_\beta R_C = -0.8$ and $R_D = 0.2$, $R_\beta R_C = -2.0$ are selected in Fig. 7 to illustrate the mixing processes in this region.

As shown in Fig. 7(a), when $1 + R_\beta R_C > 0$, the tiny fingers are generated at L2 after the initial diffusion stage. They strip dense material which is accumulated diffusively due to the faster diffusing of CO_2 . With time ongoing, these fingers strengthen, elongate, and generate a local velocity field. Initially, due to the weak velocity field, the upward fresh plumes cannot break through the barrier and move laterally under the obstruction of L1, which results in the root zipping of the fingers at L2. As the fingers merge and grow, the upward plumes become stronger, and L1 cannot prevent the upward movement of the fresh plumes. With the damage of the L1 and the development of the fresh plumes, a global velocity field is formed. However, when the upward fresh plumes reach the top boundary, they also migrate laterally under the restriction of the top boundary, resulting in the root zipping again. Initially, the zipping roots of the fingers locate at L2. After L1 is breached, the roots of the fingers are located at the top boundary. As shown in Fig. 7, this sequential merging of the fingers results in the antler-like distribution of solutes, which was not reported in previous

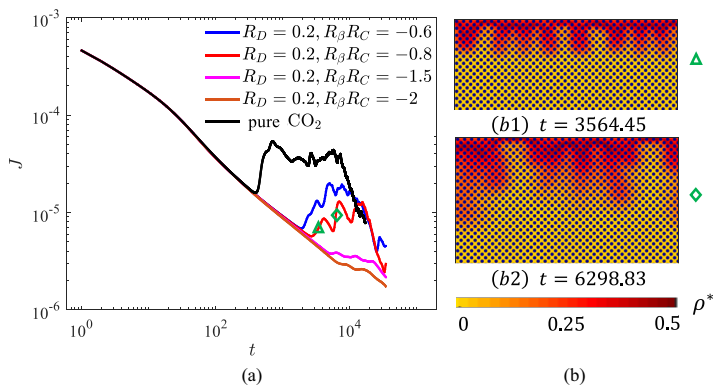


FIG. 8. Temporal dynamics of horizontally averaged dissolution flux J with different $R_\beta R_C$ and R_D in region R3.

studies. These processes can also be reflected by the profile of the dissolution flux, as shown in Fig. 8; when $1 + R_\beta R_C > 0$, both the flux growth regime are divided into two subregimes, including a early flux growth regime followed by a transitory decay process and a later flux growth regime. Early flux growth with the transitory decay is caused by the development and merging of fingers under L1, and later flux growth corresponds to the development of fingers after L1 is destroyed. The secondary increase of flux in this subregion is the most obvious difference from the pure CO₂ system.

The general phenomena for the cases with $1 + R_\beta R_C < 0$ show some differences. As shown in Fig. 7, since L1 is a layer with the lowest density in the whole system, it acts as a protective layer to isolate the top area from the overall convection; the top area cannot be affected by the upwind fresh plumes. As a result, only the solute accumulated by faster diffusion in the L2 layer is able to participate in the convective mixing process, and the solute in the top layer is largely unaffected. which have obvious effects on the overall flux of dissolution. It can be seen in Fig. 8 that, in this region, flux growth regime and subsequent regimes are no longer present, replaced by a slower period of flux decline. It means that the instability does not result in a noticeable increase in solubility in this subregion, despite the creation of convection.

Cases R4: In this region, the density profiles are monotone increasing. As shown in Fig. 2, whether in subregion (4a) or (4b), the upper fluid is less dense than the lower host fluid. Jafari Raad *et al.* [24] concluded that the system is stable in both subregions. However, in the double diffusive system, the miscible interface could be unstable when the density profile has a inflection point. It means that the convection motion is possible in subregion (4a). In a later study, Kim *et al.* [12] proved this point through the linear stability analysis. In this study, pore-scale simulations are performed to investigate the stability of the system in subregions (4a) and (4b). Simulation results with $R_D = 3, R_\beta R_C = -2$ and $R_D = 1.2, R_\beta R_C = -2$ are shown in Fig. 9. It can be seen that although the convective intensity is obviously restrained, the instability of the miscible interface could still be induced under the influence of the initial perturbations when $R_D = 3, R_\beta R_C = -2$, while the instability of the system is completely inhibited when $R_D = 1.2, R_\beta R_C = -2$. The numerical results in this section confirm the results of Kim *et al.*, which shows that when the density increases monotonically along the gravity direction, the density-driven instability would still exist in the system. To summarize, the development of the density-driven instability in an impure system can be divided into four regions based on parameters R_D and $R_\beta R_C$, where the horizontal average density demonstrates both monotonic and nonmonotonic behavior. The numerical results show that general phenomena of fingers migration in region R1 are consistent with those in pure-CO₂ system, due to the similar monotonically decreased density profile. For the cases with nonmonotonic density profiles in R2 and R3, the nonmonotony of the density profile could cause the stratification of the

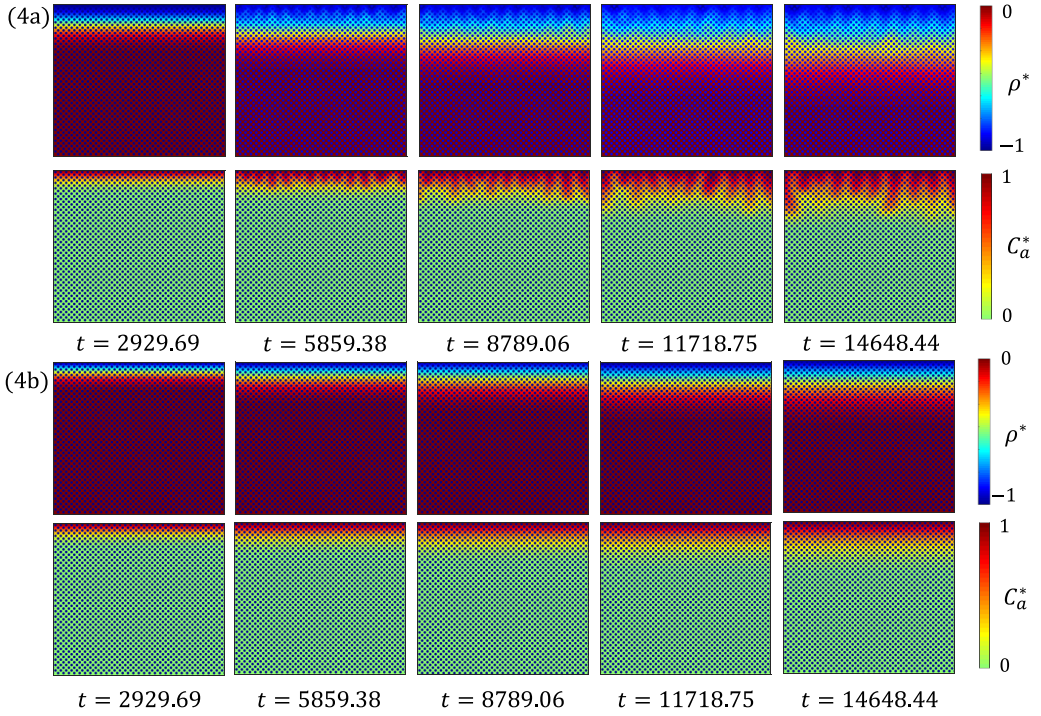


FIG. 9. Snapshots of the solute concentration profile in region R3, (4a) $R_D = 3$, $R_\beta R_C = -2$, (4b) $R_D = 1.2$, $R_\beta R_C = -2$.

density distribution, which could suppress the convective intensity of the system. Also, for region R4, where the density profile is monotonically increasing, although there is no density extremum, instability could still occur, which verifies Kim's conclusion. Compared with the exiting theoretical studies, the species distributions and some special finger patterns can be captured clearly in our pore-scale simulations.

C. The onset time of convection

As mentioned above, due to the convective mixing process, the profile of the dissolution flux at the top boundary goes through several stages, i.e., the diffusion-dominated regime, flux-growth regime, merging regime, constant flux regime, and shutdown regime. The convection caused by the growth of the perturbations in the system leads a significant increase of the dissolution flux after a period of diffusion, which shortens the time needed dissolve CO_2 completely and reduces the risk of leakage. Therefore, the onset time of convection t_{on} , which is defined as the time when the flux transitions from the diffusion-dominated to the flux-growth regime [44], is crucial in the whole process of convective mixing.

For the pure- CO_2 system, the linear stability analysis suggests that the dimensional onset time of convection is related to the Rayleigh number, which can be expressed as

$$t_{\text{on}} \approx c_0 \frac{(\phi\mu)^2 D}{(\Delta\rho H k)^2} = c_0 \frac{H^6}{D \text{Ra}^2} \sim \text{Ra}^{-2}, \quad (33)$$

where c_0 is a prefactor, which is related to the properties of the porous media and perturbations. Therefore, for a pure- CO_2 system, we can estimate the t_{on} according to the Rayleigh number and thus predict the convective mixing process of the whole system. However, for the mixing processes

with impure CO₂, the onset time t_{on} is not only related to Ra, but also influenced by impurity-related parameters such as R_D and $R_\beta R_C$, which increases the difficulty of system assessment. Therefore, an effect Rayleigh number Ra_e , which includes the effects of the other parameters mentioned above, should be defined in the impure system.

To fill this gap, in this section an intuitive, uniform expression of the efficient Rayleigh number Ra_e is given. A prefactor α is introduced to evaluate the influence of the impurities. The effective Rayleigh number Ra_e can be expressed as

$$\text{Ra}_e = \alpha \text{Ra}. \quad (34)$$

For the cases of $R_D > 1$, as analyzed above, in subregion (4b) of R4, the system is in an unconditionally stable. Therefore, when $-R_\beta R_C > R_D^{1.5}$, the definition of α can be expressed as

$$\alpha = 0, \quad R_D \geq 1, -R_\beta R_C \geq R_D^{3/2}. \quad (35)$$

In addition, in subregion (1a) of R1, region R2 and subregion (4a) of R4, the system may be unstable under the influence of the initial disturbance; for a given R_D , the closer $-R_\beta R_C$ is to $R_D^{1.5}$, the more stable the system is. Based on this concept, a uniform expression of α for the cases with $R_D \geq 0$ is given empirically as follows:

$$\alpha = \left(1 + \frac{R_\beta R_C}{R_D^{3/2}}\right)^a, \quad R_D \geq 1, -R_\beta R_C < R_D^{3/2}, \quad (36)$$

where a is a parameter related R_D , which can be fitted as $a = \ln(R_D) + 1$ according to the results of a sufficient number of numerical calculations in our present study.

For the cases with $R_D < 1$, it is difficult to give a unified expression of α according to the calculation results. Therefore, different expressions are given in different regions, respectively, and they are unified at the interface, which is selected as the profile of $R_D = (-R_\beta R_C)^{2/3}$. Then, for the parameter space with $R_D < 1$, $-R_\beta R_C < R_D^{3/2}$, the expression of α is given empirically as

$$\alpha = \left(1 + \frac{R_\beta R_C}{R_D}\right)^b, \quad R_D \leq 1, -R_\beta R_C \leq R_D^{1.5}. \quad (37)$$

Similar to a , b is also a R_D -related parameter, which can be fitted as $b = R_D$ according to the numerical results. Finally, for the cases with $-R_\beta R_C > R_D^{3/2}$, a fitting form of α is given as

$$\alpha = \left(\xi \frac{R_D^{3/2}}{-R_\beta R_C}\right)^b, \quad R_D \leq 1, -R_\beta R_C \geq R_D^{3/2}, \quad (38)$$

Since the definition of Ra_e needs to be continuous at the interface, therefore, for the limiting cases with $R_D = (-R_\beta R_C)^{2/3}$, Eqs. (37) and (38) should be consistent. Then ξ can be calculated as

$$\xi = 1 - R_D^{0.5}. \quad (39)$$

According to the definition of effective Ra_e , the onset times of convection t_{on} with different Ra_e are displayed in Fig. 10. Although the effective Rayleigh number Ra_e has empirical components, it can be seen that the calculation results of the onset time t_{on} can be well fitted as $t_{\text{on}} \sim \text{Ra}_e^{-2}$, which is consistent with the role of the Rayleigh number in a pure-CO₂ system. In addition, according to Eqs. (36) and (37), when $R_\beta R_C > 0$, the effective Rayleigh number $\text{Ra}_e > \text{Ra}$, leading to a more unstable condition. However, when $R_\beta R_C < 0$, the opposite is true. Based on this effective Rayleigh number Ra_e , we can compare the sequence of convection in different impure systems intuitively, which provides convenience for engineering applications.

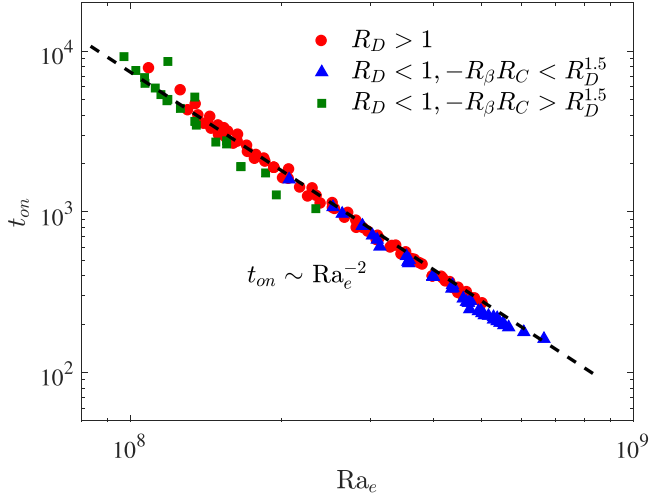


FIG. 10. Onset time of convection t_{on} in impure system with different effective Rayleigh number Ra_e .

D. Discussion with respect to CO₂ sequestration

Based on the above numerical results, we discuss several common impurities, namely, SO₂, N₂, and H₂S, in this subsection. As a common pollutant emitted by coal-fired power plants, the solubility of SO₂ in water is significantly greater than that of CO₂, which leads to the fact that the influence of SO₂ cannot be ignored when considering the trapping mechanisms with respect to the short-term and/or long-term geological storage of CO₂. The diffusion rate of SO₂ is substantially slower than that of CO₂ in brine, and it can significantly increase the density of the combined solution. Therefore, the density distribution of a CO₂-SO₂ system in the diffusion stage can be assigned to region 1b (as shown in Fig. 11), where the density is monotonically decreasing in the gravity direction while the system Rayleigh number is clearly increasing. In this region, the convection

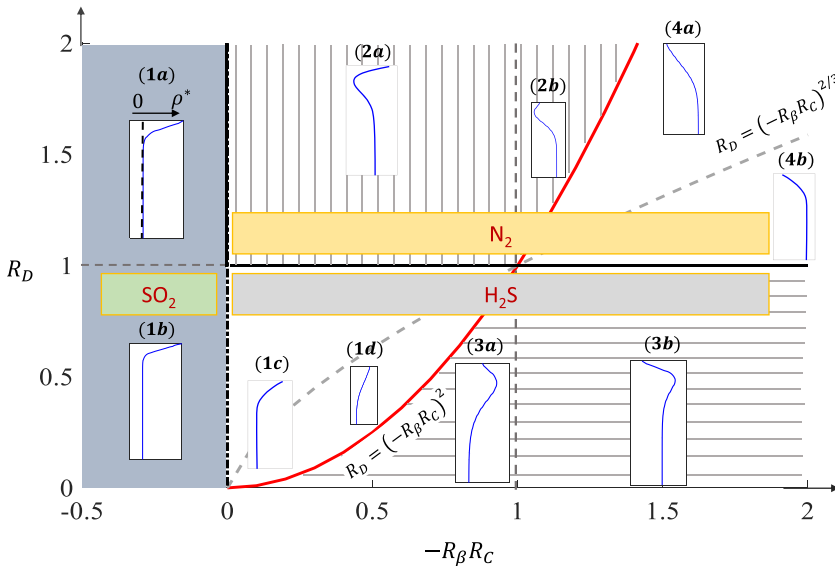


FIG. 11. Classification of SO₂, N₂, and H₂S based on the parameter space $(-R_\beta R_C, R_D)$.

starts earlier and the mixing intensity increases. In this sense, SO_2 is advantageous for increasing the effectiveness of CO_2 dissolution and storage in the system.

As for the H_2S impurity, the mixed solution is slightly denser than salt water after it dissolves in water, and its diffusion coefficient in salt water is lower than that of CO_2 . Therefore, depending on the physical properties of H_2S , it can be assigned to regions 1 and 3 (as shown in Fig. 11). The analysis in this paper indicates that at these two intervals the presence of impurity will inhibit the instability and prolong the convective onset time. From this perspective, the presence of H_2S is not conducive to the dissolution and storage of CO_2 .

N_2 is the main impurity of the CO_2 streams no matter which carbon capture technology is employed. Its influence on the density of a mixed solution is similar to that of H_2S , but its diffusion coefficient is slightly larger, so it can be assigned to regions 2 and 4 depending on the physical properties of N_2 . Similarly to H_2S , the presence of N_2 in these regions will delay the onset time of convection and have an adverse effect on CO_2 dissolution sequestration.

It should be emphasized that the above discussion is based on an ideal situation in the present study. In fact, during the storage process, impurities have various effects on the security and effectiveness of storage. Take nitrogen, for example: N_2 monitoring can be utilized as a safety alarm for leakage while giving time for leak remediation because N_2 moves in the leading edge of the injected gas. Furthermore, N_2 also improves the mobility and propagation of the gas stream throughout the injection time [26]. In this way, solubility trapping could be enhanced by increasing the surface area between the injected gas mixture and brine. Consequently, while referring to the results of this paper, we also need to properly take into account the impact of other aspects when analyzing the impact of impurities with actual CO_2 sequestration work.

V. CONCLUSION

Pore-scale simulations of a density-driven convective mixing process in brine sequestration of impure CO_2 have been conducted in a two-dimensional isotropic synthetic porous medium. The behaviors of the density profile with depth are classified first. Based on the different density distributions, the system could be divided into four regions in the parameter space ($-R_\beta R_C$, R_D), and the nonlinear simulations are performed from the initial diffusion to almost solute saturated state of the computational domain in these four different regions. First, for the cases in region R1, where the density profiles are monotone decreasing, the general phenomena of the mixing processes are consistent with those in the pure- CO_2 system due to the similar morphology of the density profile. For region R2, the system density could form a layered structure with a minimum located at the middle layer. In this scenario, the instability occurs at the top layer, and the bottom layer acts as a barrier, hindering the development of convection. Particularly, when $1 + R_\beta R_C < 0$, the fingers generated at the upper layer could not break through the barrier of L3, and the convection is confined to the top region. For the R3 region, the density of the system displays a stratification with a local maximum at middle layer. For the cases in this region, the fingers are developed at the interface between the middle and bottom layers, and the top layer inhibits the fresh plume from carrying solute to the bottom, thus greatly affecting the promotion of convection on the dissolution rate. Finally, for region R4, where the density profile is monotone increasing. Although there is no density extremum, when the density profile has an inflection point, instability will still occur, which is consistent with the previous theory analysis.

In addition, an effective Rayleigh number Ra_e is presented in this paper. Consistent with a pure- CO_2 system, the onset time of convection t_{on} can be well fitted as $t_{\text{on}} \sim \text{Ra}_e^{-2}$. Therefore, based on this effective Rayleigh number Ra_e , we can roughly estimate the onset time of convection, and combined with the previous nonlinear simulation results, we can make a simple prediction of any convective mixing process involving impurities, which provides great convenience for engineering applications.

ACKNOWLEDGMENT

This work was supported by the National Natural Science Foundation of China (No. 51836003). No conflict of interest is declared.

- [1] S. Solomon, D. Qin, M. Manning, Z. Chen, M. Marquis, K. B. Averyt, M. Tignor, H. L. Miller, S. Solomon, and D. Qin, *Climate change 2007: Synthesis Report. Contribution of Working Group I, II and III to the Fourth Assessment Report of the Intergovernmental Panel on Climate Change, Summary for Policymakers*. [M]. Switzerland, 2007.
- [2] D. Wang, B. Dong, S. Breen, M. Zhao, J. Qiao, Y. Liu, Y. Zhang, and Y. Song, Approaches to research on CO₂/brine two-phase migration in saline aquifers, *Hydrogeol. J.* **23**, 1 (2015).
- [3] P. M. Cox, R. A. Betts, C. D. Jones, S. A. Spall, and I. J. Totterdell, Acceleration of global warming due to carbon-cycle feedbacks in a coupled climate model, *Nature (London)* **408**, 184 (2000).
- [4] T. Ajayi, J. S. Gomes, and A. Bera, A review of CO₂ storage in geological formations emphasizing modeling, monitoring and capacity estimation approaches, *Petrol. Sci.* **16**, 1028 (2019).
- [5] J. C. Stephens and B. van der Zwaan, *CO₂ capture and storage (CCS): Exploring the research, development, demonstration, and deployment continuum, Discussion Paper, 2005-08, Belfer Center for Science and International Affairs*, Harvard Kennedy School, 2005.
- [6] J. Gibbins and H. Chalmers, Carbon capture and storage, *Energy Policy* **36**, 4317 (2008).
- [7] R. Korbøl and A. Kaddour, Sleipner Vest CO₂ disposal-injection of removed CO₂ into the Utsira formation, *Energy Conversion Manage.* **36**, 509 (1995).
- [8] M. Grobe, J. C. Pashin, and R. L. Dodge, *Carbon Dioxide Sequestration in Geological Media: State of the Science* (American Association of Petroleum Geologists, Tulsa, USA, 2009).
- [9] G. Weir, S. P. White, and W. M. Kissling, Reservoir storage and containment of greenhouse gases, *Transp. Porous Media* **23**, 37 (1996).
- [10] J. Ennis-King and L. Paterson, Rate of dissolution due to convective mixing in the underground storage of carbon dioxide, in *Greenhouse Gas Control Technologies—6th International Conference* (Pergamon, Oxford, 2003), Vol. I, pp. 507–510.
- [11] X. Ji and C. Zhu, Predicting possible effects of H₂S impurity on CO₂ transportation and geological storage, *Environ. Sci. Technol.* **47**, 55 (2013).
- [12] M. C. Kim and K. H. Song, Effect of impurities on the onset and growth of gravitational instabilities in a geological CO₂ storage process: Linear and nonlinear analyses, *Chem. Eng. Sci.* **174**, 426 (2017).
- [13] L. E. Crandell, B. R. Ellis, and C. A. Peters, Dissolution potential of SO₂ co-injected with CO₂ in geologic sequestration., *Environ. Sci. Technol.* **44**, 349 (2010).
- [14] D. Li and X. Jiang, Numerical investigation of convective mixing in impure CO₂ geological storage into deep saline aquifers, *Int. J. Greenhouse Gas Control* **96**, 103015 (2020).
- [15] D. Li and X. Jiang, Numerical investigation of the partitioning phenomenon of carbon dioxide and multiple impurities in deep saline aquifers, *Appl. Energy* **185**, 1411 (2017).
- [16] D. Li, H. Zhang, L. Yang, W. Xu, and J. Xi, Effects of N₂ and H₂S binary impurities on CO₂ geological storage in stratified formation—A sensitivity study, *Appl. Energy* **229**, 482 (2018).
- [17] A. Riaz, M. Hesse, H. Tchelepi, and F. Orr, Onset of convection in a gravitationally unstable diffusive boundary layer in porous media, *J. Fluid Mech.* **548**, 87 (2006).
- [18] T. F. Faisal, S. Chevalier, and M. Sassi, Experimental and numerical studies of density driven natural convection in saturated porous media with application to CO₂ geological storage, *Energy Procedia* **37**, 5323 (2013).
- [19] A. C. Slim, M. M. Bandi, J. C. Miller, and L. Mahadevan, Dissolution-driven convection in a Hele–Shaw cell, *Phys. Fluids* **25**, 024101 (2013).
- [20] T. Lei and K. H. Luo, Pore-scale study of dissolution-driven density instability with reaction $A + B \rightarrow C$ in porous media, *Phys. Rev. Fluids* **4**, 063907 (2019).

- [21] J. Wang, D. Ryan, E. J. Anthony, and T. Aikrn, Effects of impurities on CO₂ transport, injection and storage, *Energy Procedia* **4**, 3071 (2011).
- [22] D. Li and X. Jiang, A numerical study of the impurity effects of nitrogen and sulfur dioxide on the solubility trapping of carbon dioxide geological storage, *Appl. Energy* **128**, 60 (2014).
- [23] D. Li, X. Jiang, Q. Meng, and Q. Xie, Numerical analyses of the effects of nitrogen on the dissolution trapping mechanism of carbon dioxide geological storage, *Comput. Fluids* **114**, 1 (2015).
- [24] S. M. Jafari Raad and H. Hassanzadeh, Does impure CO₂ impede or accelerate the onset of convective mixing in geological storage? *Int. J. Greenhouse Gas Control* **54**, 250 (2016).
- [25] S. Mahmoodpour, B. Rostami, and H. Emami-Meybodi, Onset of convection controlled by N₂ impurity during CO₂ storage in saline aquifers, *Int. J. Greenhouse Gas Control* **79**, 234 (2018).
- [26] S. Mahmoodpour, M. A. Amooie, B. Rostami, F. Bahrami, H. Lund, and M. J. Kaiser, Effect of gas impurity on the convective dissolution of CO₂ in porous media, *Energy* **199**, 117397 (2020).
- [27] S. Omrani, S. Mahmoodpour, B. Rostami, and I. S. MehdiSalehi Sedeh, Diffusion coefficients of CO₂–SO₂–water and CO₂–N₂–water systems and their impact on the CO₂ sequestration process: Molecular dynamics and dissolution process simulations, *Greenhouse Gases: Sci. Technol.* **11**, 764 (2021).
- [28] A. M. Tartakovsky, G. D. Tartakovsky, and T. D. Scheibe, Effects of incomplete mixing on multicomponent reactive transport, *Adv. Water Resour.* **32**, 1674 (2009).
- [29] S. M. Jafari Raad, H. Hassanzadeh, and J. Ennis-King, On the dynamics of two-component convective dissolution in porous media, *Water Resour. Res.* **55**, 4030 (2019).
- [30] M. C. Kim and K. H. Song, Gravitational instability and its scaling relation of a partially miscible two-component system in a porous medium, *Int. J. Heat Mass Transf.* **169**, 120899 (2021).
- [31] N. Tilton, Onset of transient natural convection in porous media due to porosity perturbations, *J. Fluid Mech.* **838**, 129 (2018).
- [32] G. S. Pau, J. B. Bell, K. Pruess, A. S. Almgren, M. J. Lijewski, and K. Zhang, High-resolution simulation and characterization of density-driven flow in CO₂ storage in saline aquifers, *Adv. Water Resour.* **33**, 443 (2010).
- [33] J. P. Ennis-King and L. Paterson, Role of convective mixing in the long-term storage of carbon dioxide in deep saline formations, *SPE J.* **10**, 349 (2003).
- [34] Z. Guo, B. Shi, and N. Wang, Lattice BGK model for incompressible Navier-Stokes equation, *J. Comput. Phys.* **165**, 288 (2000).
- [35] R. Du, B. Shi, and X. Chen, Multi-relaxation-time lattice Boltzmann model for incompressible flow, *Phys. Lett. A* **359**, 564 (2006).
- [36] X. He and L. S. Luo, Lattice Boltzmann model for the incompressible Navier–Stokes equation, *J. Stat. Phys.* **88**, 927 (1997).
- [37] Z. Guo, C. Zheng, and B. Shi, Discrete lattice effects on forcing terms in the lattice Boltzmann method, *Phys. Rev. E* **65**, 046308 (2002).
- [38] Q. Liu, Y. He, Q. Li, and W. Tao, A multiple-relaxation-time lattice Boltzmann model for convection heat transfer in porous media, *Int. J. Heat Mass Transf.* **73**, 761 (2014).
- [39] L. Ju, B. Shan, Z. Yang, and Z. Guo, An exact non-equilibrium extrapolation scheme for pressure and velocity boundary conditions with large gradients in the lattice Boltzmann method, *Comput. Fluids* **231**, 105163 (2021).
- [40] T. Lei and K. H. Luo, Differential diffusion effects on density-driven instability of reactive flows in porous media, *Phys. Rev. Fluids* **5**, 033903 (2020).
- [41] M. Jotkar, L. Rongy, and A. D. Wit, Reactive convective dissolution with differential diffusivities: Nonlinear simulations of onset times and asymptotic fluxes, *Phys. Rev. Fluids* **5**, 104502 (2020).
- [42] C. Chen and D. Zhang, Pore-scale simulation of density-driven convection in fractured porous media during geological CO₂ sequestration: Pore-scale study of density-driven flow, *Water Resour. Res.* **46**, 11 (2010).
- [43] L. Ju, B. Shan, P. Liu, and Z. Guo, Pore-scale study of miscible density-driven mixing flow in porous media, *Phys. Fluids* **33**, 034113 (2021).
- [44] J. T. H. Andres and S. S. S. Cardoso, Onset of convection in a porous medium in the presence of chemical reaction, *Phys. Rev. E* **83**, 046312 (2011).